Researchers Journal of Science and Technology (REJOST)
https://rejost.com.ng

Analysis of the local wave vector orientation of plasma waves in the Earth's Magnetosheath observed by spacecraft in the tetrahedral formation

Ekong Ufot Nathaniel[*1], Uduakobong S. Imo[2], Jewel E. Thomas[1]

Received: February 19, 2024 /Accepted: April 21, 2024

Abstract

Spacecraft architecture that places the spacecraft in a tetrahedral arrangement rather than in the same plane has been taken into consideration in this analysis. The combination of the empirical mode technique and the simple Hilbert transform have been used on the real-valued signal observed aimed at analyzing the local wave vector orientation of plasma waves in the Earth's Magnetosheath observed by spacecraft in the tetrahedral formation. The real-valued signal is decomposed into intrinsic mode functions (imf). The tetrahedral geometry of the four Cluster satellite on February 18, 2002, observed at 5: 27: 30 UT, yielded average values of tetrahedron elongation E = 0.070 and planarity P = 0.040 for a scale of 20.000km: 1.000cm. Since the values of E and P for a regular tetrahedron are close to zero, these values are small enough to ensure good results of the 3-D measurement. This produced results in three dimensions along the separation of each satellite pair. The result reveals at some points, a non-dispersive wave. The projections of the wave vector that make angles with the spacecraft separation line enabled the determination of wave orientation with respect to the sun using the solar wind coordinate system. In addition, these angles specify the wave vector's direction. The average minimum and maximum spacecraft separation, according to the results, were 88 and 108 km, respectively. The average value of the plasma bulk velocity during the chosen period is [−175,52, 112] kms^{-1} in x, y and z directions respectively. The local wave vector projection has been plotted along the spacecraft separation. As a reference satellite, we used Cluster satellite C3. This made it possible to pair, and Sat13, Sat23, and Sat43 were used. The wave's wavelength is between 1030.2 and 1366.1 kilometers. Between the separation line of the Sat13 pair and the projection of each wave vector component, there is an angle that ranges from 87 to 91 degrees. With the use of tetrahedral

formation of spacecraft to analyze the local wave vector orientation of plasma waves in the Earth's Magnetosheath, we believe the wave to be spiral-shaped wave.

✉ Ekong Ufot Nathaniel: ekongnath@yahoo.com

[1]Department of Physics, Akwa Ibom State University, Ikot Akpaden, Nigeria

[2]Department of Physics, University of Uyo, Uyo, Nigeria

Keywords: Magnetosheath**;** Plasma Waves; Instantaneous Frequency; local wave vector; solar wind.

1.0 Introduction

The ability to obtain 3D wave vectors from space plasma observations has been made possible by the launch of the Cluster II spacecraft. For each gathered real-valued signal, the instantaneous local wave vector analysis relies on a complex-valued signal that is analytically treated (Gabor, 1946; Huang, *et al*., 1998; Rilling and Flandrin, 2006; Carozzi, 2004). Cluster II four-point observations offer a rare opportunity to identify different wave properties. For the purpose of determining the plasma wave's instantaneous frequency (Boashash, 1992; Nathaniel *et al*., 2013 and Nathaniel *et al*., 2016), the empirical mode technique (Huang *et al*., 1998) and the simple Hilbert transform (Flandrin *et al*., 2004; Huang *et al*., 2005; Rilling and Flandrin, 2006; Nathaniel *et al*., 2016) have been combined. Thus, we utilize this method to obtain an analytical depiction of a real-valued signal. Numerous methods have been considered for the analysis of spatiotemporal behavior in space (Paschmann, *et al*., 1998). One method takes into account the instantaneous local wave vector and relies on the assumption of a mono-component signal after filtering and applying basic Hilbert analysis (Carozzi, 2004). It takes more than two spacecraft configurations, such as the Cluster II mission, to determine the wave vector for meaningful results. Additional calculations have established the three-dimensional structure of plasma dynamics based on assumptions about the stationarity and linearity of the signal and the application of phase differencing techniques (Balikhin *et al*., 1997a; Balikhin *et al*., 1997b; Walker *et al*., 2004) and the K-filtering method (Pincon *et al*., 1991; Glassmeier *et al*., 2001). We are utilizing electric field data similarly to that of Walker *et al*. (2004) and magnetic field data similar to that of Carozzi *et al*. (2004), whose estimated instantaneous local wave vector was based on filtering.

For both single and multiple probes (Beall *et al*., 1982; Carozzi, 2004), the instantaneous wave vector is given as the spatial gradient of the phase with time. For the multi-probe case, as applied to Cluster II observations, it is given as**:**

$$\boldsymbol{k_i}(\boldsymbol{\sigma}) = -\frac{\boldsymbol{d_x}^{(\alpha,1)}\boldsymbol{\theta_i}^{(\alpha)}(\boldsymbol{\sigma})}{\boldsymbol{d_x}^{(\alpha,1)}\vec{\boldsymbol{x}}^{(\alpha)}(\boldsymbol{\sigma})} \qquad (1)$$

In x y z, $\boldsymbol{k_i} = \begin{pmatrix} k_x \\ k_y \\ k_z \end{pmatrix}$ (2)

Using C_3 as a reference spacecraft,

$$\boldsymbol{d_x}^{(\alpha,1)}\vec{\boldsymbol{x}}^{(\alpha)}(\boldsymbol{\sigma}) \equiv \begin{pmatrix} x^{(1)-(3)} & y^{(1)-(3)} & z^{(1)-(3)} \\ x^{(2)-(3)} & y^{(2)-(3)} & z^{(2)-(3)} \\ x^{(4)-(3)} & y^{(4)-(3)} & z^{(4)-(3)} \end{pmatrix} \qquad (3)$$

$$\boldsymbol{d_x}^{(\alpha,1)}\boldsymbol{\theta_i}^{(\alpha)}(\boldsymbol{\sigma}) = \begin{pmatrix} \theta_i{}^{(1)} - \theta_i{}^{(3)} \\ \theta_i{}^{(2)} - \theta_i{}^{(3)} \\ \theta_i{}^{(4)} - \theta_i{}^{(3)} \end{pmatrix} \qquad (4)$$

where σ stands for the sample point, α indicates the cluster satellites (C_1, C_2, C_3, and C_4), and i is an integer on the intrinsic mode function (imf) (i = 1,2,3,..., n). The instantaneous wave vector is computed using equation 1. Its component is computed using equation 2 and the spacecraft separation distances are calculated using equation 3. The phase difference was computed using equation 4. Balikhin *et al*. (2003) addressed the conversion of non-orthogonal projection coordinates to physical coordinates (Geocentric Solar Magnetospheric (GSM), Geocentric Solar Ecliptic (GSE), etc.). In this work, we handle Â for every sample, which yields a 3×3 matrix from the satellite pair separations that, in accordance with Nathaniel *et al*. (2013) and the reference therein, is linearly independent. The transformation matrix Â, which is derived from the satellite pair separation distances, is also utilized to create non-orthogonal basis vectors, as per the adoption from Balihkin *et al.* (2003). The wave vector's computed projection along the satellite separation is used to calculate the instantaneous wave vector, or k.$\hat{A}$ is expressed as:

$$\hat{A}\mathrm{k} = \check{k} \qquad (5)$$

where

$$\mathrm{k} = [\hat{A}]^{-1}\check{k} \qquad (6)$$

$$\check{k} = [k1, k2, k3]$$

where the pairs sat13, sat23, and sat43 are denoted by 1, 2, and 3. Whereas $\check{k}$ is the instantaneous wave vector projection along satellite pair separations, computed k is the instantaneous wave vector. Since the minimum wavelength of waves is greater than the minimum distance between spacecraft, the estimated wave vectors are predicated on this assumption. The aim of this work is to analyze the local wave vector orientation of plasma waves in the Earth's Magnetosheath observed by spacecraft in the tetrahedral formation.

2.0 Materials and Method

In this work, four FGM instruments from the Cluster (C_1, C_2, C_3, and C_4) spacecraft were used to collect data (Balogh *et al*., 1997). As shown in Figures 1 and 2 below, the magnetic field data were collected during the time the spacecraft were leaving the magnetopause and heading towards the magnetosheath. They were also taken into consideration when the spacecraft was getting close to the bow shock. Using the enhanced empirical mode decomposition (EMD) technique, the magnetic field was broken down (Rilling and Flandrin 2006; Huang *et al*., 2003, Huang *et al*., 2005, Flandrin *et al*., 2004). The purpose of this was to remove the noise contribution from the data, which needs to be carefully considered, and extract the various oscillatory modes known as intrinsic mode functions (imf) that make up the data. The spectrogram was used to view the average frequency content in each of the extracted modes, and the scalogram was used to view the average frequency's time instant in accordance with the findings (Nathaniel *et al.*, 2013). This selection was made as a step of confirmation, providing a preview of the instantaneous frequency. In order to remove noise, empirical mode decomposition (EMD) and wavelet were combined (Helong *et al*., 2007). EMD has been verified as a dyadic filter through the noise removal process (Huang *et al*., 2003; Flandrin *et al*., 2004).

The information was collected during the time frame that Walker *et al*. (2004) used in their analysis to determine the primary wave mode. This analysis used the assumption of linear and stationary behavior to compare its results, which are based on waveforms reflecting non-linear and non-stationary behavior, with those of Walker *et*

al. (2004). All four spacecrafts have a spin axis that is 84 degrees latitude (in the GSE coordinate). This axis provides an equivalent representation of the GSE frame that rotates 180 degrees around the X-axis (Walker *et al*., 2004). The goal of this work is to analyze the magnetosheath's instantaneous local wave vector. The direction of the magnetic field normal to bow shock was ascertained by using downstream data near the shock (Sonnerup and Cahill 1967). Data were collected on February 18, 2002, between 06:05:19 and 06:28:41 UT, in order to determine the shock normal (Balogh *et al.* (2005); Svenningsson *et al*. (2022)). For data collected between 04:55:00 and 05:18:20 UT, Figure 1 shows the magnetic field profile as the spacecraft are heading outward from the magnetosphere towards the magnetosheath. At 04:59:00 UT, the magnetopause was crossed. These were gathered from the observations of the Cluster (C_1, C_2, C_3, and C_4) spacecraft's four Flux Gate Magnetometer (FGM)instruments. Data from C1 (red), C_2 (black), C_3 (blue), and C_4 (magenta) are represented by the various colors. Panels display the magnetic field's magnitude as well as its X, Y, and Z components in GSE coordinates from top to bottom. Additionally, the magnetic field profile for the magnetosheath data chosen to determine the shock normal is shown in Figure 2. The shock normal was determined using the minimum variance method. The information was gathered from the observations of the C_1, C_2, C_3, and C_4 spacecraft's four FGM instruments in the Cluster. In order to analyze the local wavevector (k), we collected data in the bow shock's downstream region (the Magnetosheath) between 05:15:00 and 05:35:00 UT.

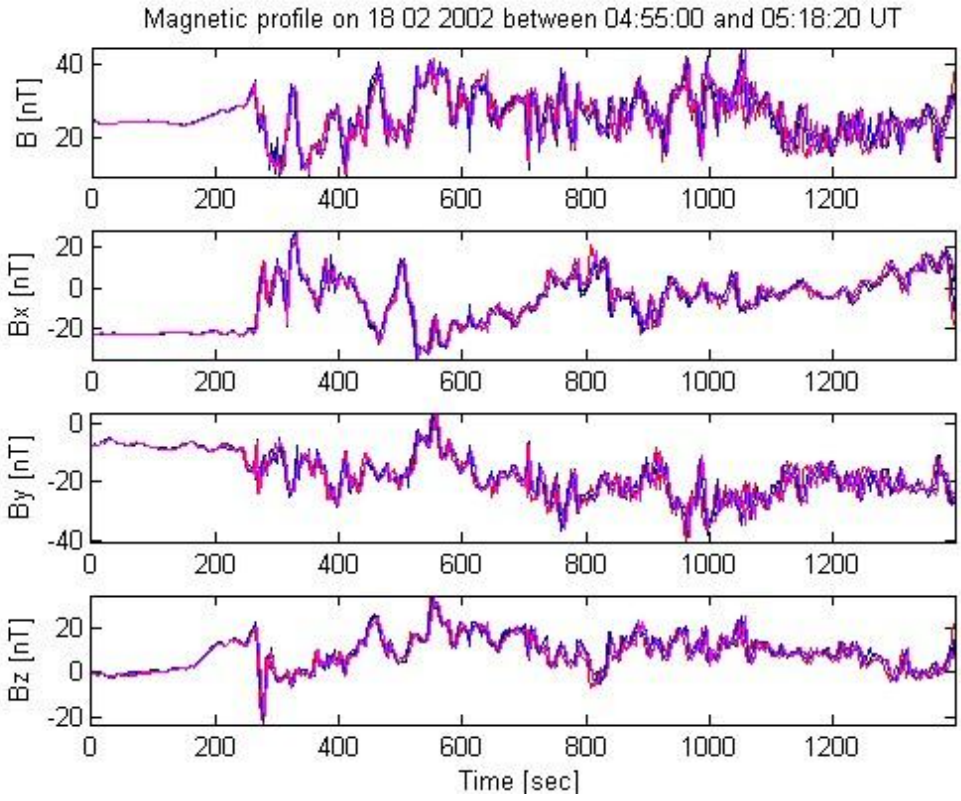

Figure 1: The magnetic field profile as the spacecraft leaves the magnetopause and moves toward the magnetosheath. These were gathered from the observations of the Cluster (C_1, C_2, C_3, and C_4) spacecraft's four FGM instruments. Data

from C_1 (red), C_2 (black), C_3 (blue), and C_4 (magenta) are represented by the various colors. Panels display the magnetic field's magnitude as well as its X, Y, and Z components in GSE coordinates from top to bottom (http://cdaweb.gsfc.nasa.gov/cgi-bin/eval2.cgi).

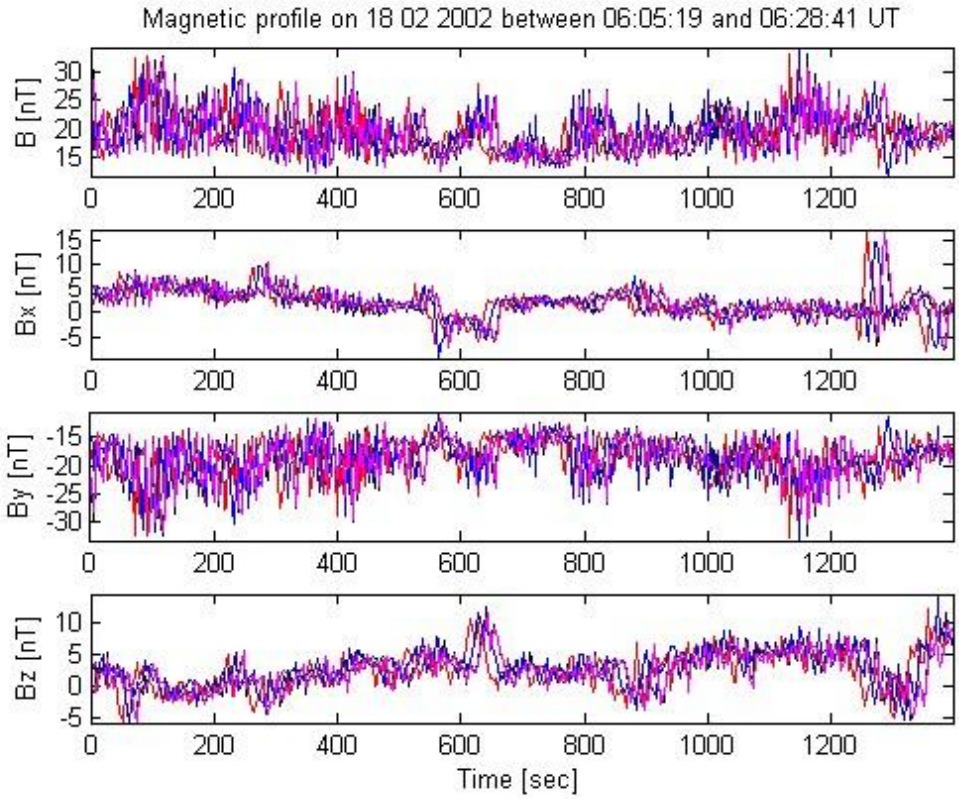

Figure 2: The magnetic profile for the magnetosheath data that was obtained near the bow shock and used to calculate the shock normal. It was gathered from the observations of the C_1, C_2, C_3, and C_4 spacecraft's four FGM instruments. Data from C_1 (red), C_2 (black), C_3 (blue), and C_4 (magenta) are represented by the various colors. Panels display the magnetic field's magnitude as well as its X, Y, and Z components in GSE coordinates (http://cdaweb.gsfc.nasa.gov/cgi-bin/eval2.cgi).

3.0 Results

Figures 3-5 display the tetrahedral geometry of the four Cluster spacecrafts C_1 (red), C_2 (black), C_3 (blue) and C_4 (magenta). The chosen geometries are considered based on their small values of tetrahedron elongation E and planarity P.A scale of 20 km = 1 cm is used for spacecraft separation. The spacecraft separation averaged 88 km at the minimum and 108 km at the maximum. For an efficient 3-D analysis of the local wavevector, the two primary parameters of the spacecraft's tetrahedral geometry, the tetrahedron elongation E and the planarity P were taken into account. According to Robert et al. (1998), their average values were E = 0.076 ± 0.006 and P = 0.053 ± 0.004. Since the values of E and P for a regular tetrahedron is close to zero, these values were small enough to ensure good results of the 3 − D measurement.

The different tetrahedral geometries that have been chosen to compare with our selections and validate our data are displayed in Figures 3 through 5. For a scale of 20.000km: 1.000cm, Figure 3 displays a tetrahedral pattern for data collected at 04:55:30 UT with E = 0.180 and P = 0.130. Where C4=green, C1=blue, C2=red, and

C3=black. For data collected at 05:58:30 UT, Figure 4 displays a tetrahedral pattern with E = 0.020 and P = 0.003. Additionally, a pattern supporting E = 0.070 and P = 0.040 for data collected at 05: 27: 30 UT is shown in Figure 5. Since E and P are both extremely small and nearly equal to zero, as previously stated, we are utilizing the models shown in Figures 4 and 5. The average value of the plasma bulk velocity during the chosen period is −175 km/s in x direction, 52 km/s in y direction and 112 km/s in z direction. This is calculated from values in Table 1 below. Table 1 shows the frequency, components, and magnitude of the plasma bulk velocity between 05:15:30 and 05:35:30 UT on February 18, 2002. For the x− component of the data, the mean and standard errors on the frequencies f1 and f2 are, respectively, 0.0337 ± 0.0004 Hz and 0.0180 ± 0.0001 Hz.

The Eigen vectors of minimum variance for each of the utilized spacecraft are displayed in Table 2. Illustration of the direction of the maximum, intermediate, and minimum variance using C_1 is shown in Table 3. Eigen vectors displaying the magnetic minimum, intermediate, and maximum variance directions at the bow shock normal is displayed in Figure 6. Figure 7 is side view of Figure 6. The angles for data collected between 05:15:30 and 05:35:30 UT between the spacecraft's separation line and the wave vector projection are shown on Table 4. Components of wave vector along the separation of spacecraft are shown on Table 5. C3 is the spacecraft used as a reference spacecraft. Instantaneous wave vector for 35 MHz mean frequency wave propagation, expressed in $(\text{kilometers})^{-1}$ is displayed on Table 6.

Figure 8 displays the instantaneous projection of wave vector along sat13 separation. Figure 9 displays the wave vector projected instantly along the Sat23 separation. Figure 10 shows the wave vector projected instantly along the Sat43 separation. Figure 11 shows wave vector projection's elevation and contour along the Sat23 separation. Figure 12 shows the wave vector's elevation and contour along the Sat43 separation. Figure 13 shows the wave vector's elevation and contour along the Sat13 separation. The plot of the instantaneous wave number against time is shown in Figure 14. This plot shows the correlation between Sat 1 (blue) and Sat 4 (green), whereas Sat 2 (red) is anti-correlated with Sat 4. Similarly, Figures 15–20 provide the distributions in x and z – components, and the contour of the wave vector projection in y and x components.

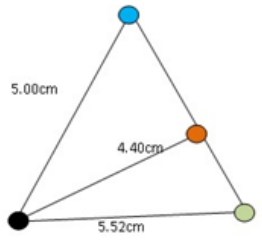

Figure 3: The four Cluster spacecraft's tetrahedral geometry on February 18, 2002, at 04:55:30 UT. C1 is blue, C2 is red, C3 is black, and C4 is green. P = 0.13 and E = 0.18.

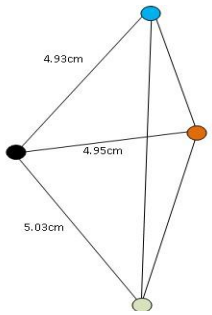

Figure 4: Tetrahedral geometry diagram of the four Cluster spacecraft on February 18, 2002, at 05:58:30 UT, with E=0.020 and P=0.003.

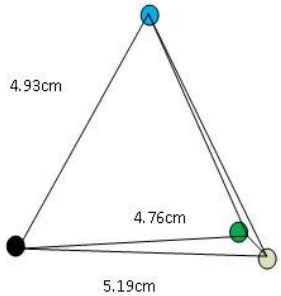

Figure 5: The four Cluster spacecraft's tetrahedral geometry on February 18, 2002, at 05:27:30 UT. P=0.040, E=0.070.

Table 1: Frequency, components, and magnitude of the plasma bulk velocity between 05:15:30 and 05:35:30 UT on February 18, 2002

t [h:m:s]	f1 [Hz]	f2 [Hz]	V_x [kms^{-1}]	V_y [kms^{-1}]	V_z [kms^{-1}]	| V | [kms^{-1}]
05:15:30	0.051	0.049	-210	56	124	250
05:16:30	0.051	0.065	-191	32	116	226
05:17:30	0.061	0.069	-161	34	111	199
05:18:30	0.062	0.052	-215	116	120	272
05:19:30	0.062	0.043	-269	140	155	340
05:21:30	0.058	0.035	-211	43	126	249
05:22:30	0.057	0.033	-195	28	102	222
05:23:30	0.059	0.035	-188	42	120	227
05:24:30	0.064	0.039	-185	35	125	226
05:25:30	0.070	0.044	-179	43	120	219
05:26:30	0.076	0.056	-171	39	115	209
05:27:30	0.072	0.055	-198	35	132	240
05:28:30	0.065	0.053	-174	33	122	215
05:29:30	0.057	0.045	-165	40	126	211
05:30:30	0.048	0.037	-159	36	133	211
05:31:30	0.040	0.029	-174	33	117	212
05:32:30	0.017	0.021	-187	38	137	235
05:33:30	0.043	0.021	-176	36	125	219
05:34:30	0.043	0.021	-181	39	128	225
05:35:30	0.044	0.021	-184	33	125	225

Table 2: The Eigen vectors of minimum variance for each of the utilized spacecraft. Spacecraft four is displayed in the first column

Spacecraft (Instruments: FGM)	Eig.vector [nT] X Y Z	Eig.value [nT]^2	Std. dev. on eig.values
C_1	0.889, 0.458, -0.014	1.616	1.271
C_2	0.859, 0.510, -0.036	1.741	1.319
C_3	0.896, 0.443, 0.023	1.834	1.354
C_4	0.905, 0.425, 0.040	1.946	1.395

Table 3: Using Cluster C1, illustrating the direction of the maximum, intermediate, and minimum variance

I	Eig.val [nT]^2	Eig.vec x1X [nT]	Eig.vec x2Y [nT]	Eig.vec x3Z [nT]	<B >xi [nT]
1	1.616	0.889	0.458	-0.014	8.474
2	10.144	-0.232	425	-0.875	4.364
3	17.227	-0.395	0.781	0.484	-0.132

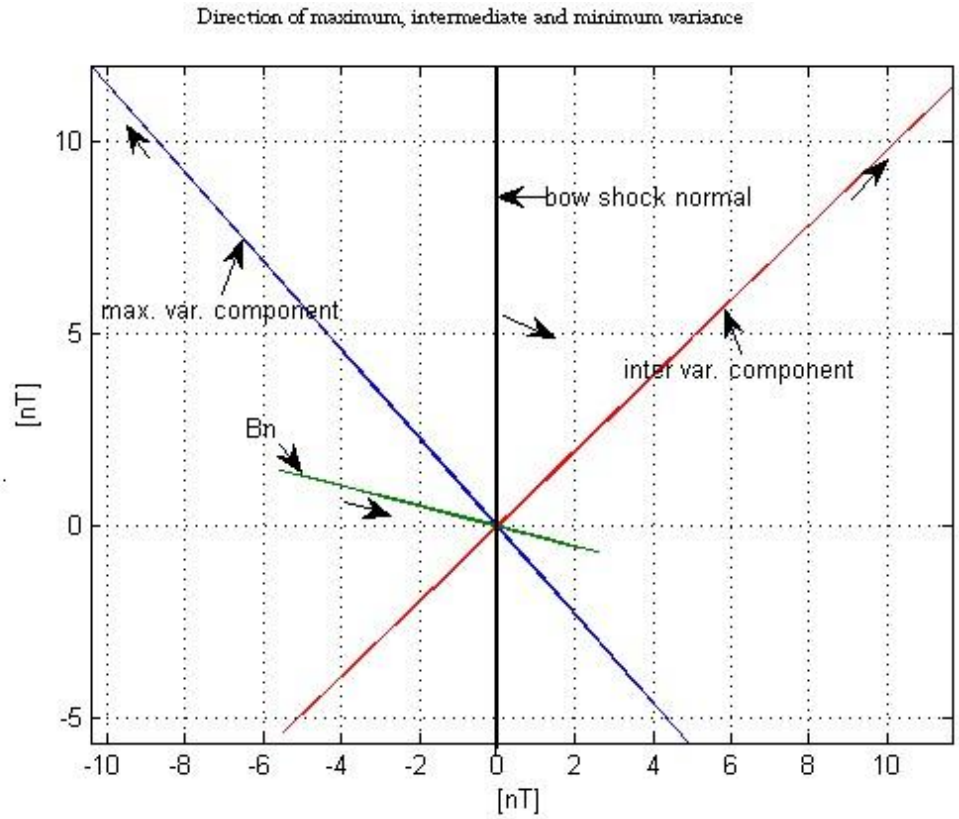

Figure 6: Eigen vectors displaying the magnetic minimum, intermediate, and maximum variance directions at the bow shock normal. During the traversal of the bow shock by Cluster spacecraft C1 on February 18, 2002, from 06:05:31 to 06:28:41 UT, it also demonstrates the orthogonality of the three components, which consist of one normal and two tangential components.

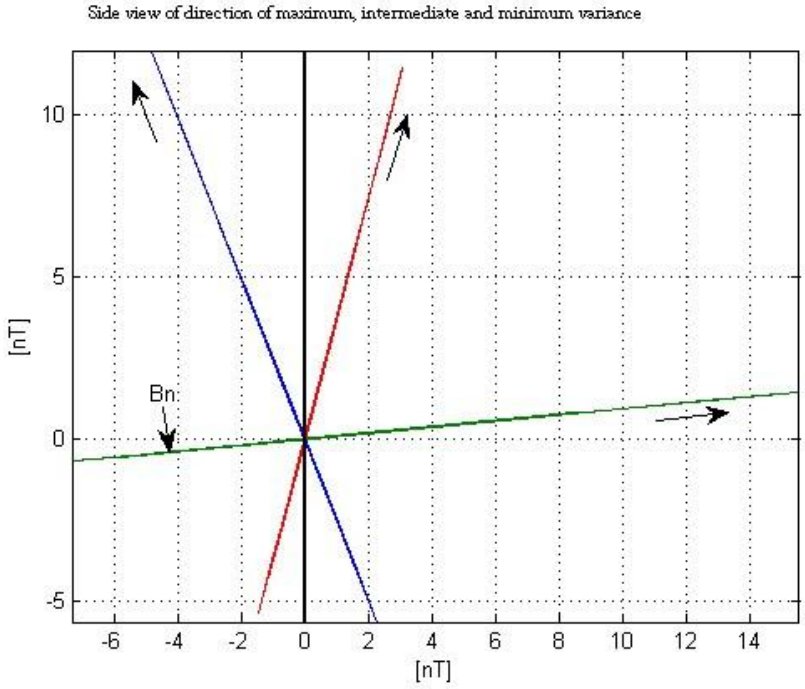

Figure 7: The Eigen vectors' maximum, intermediate, and minimum variances from a side view

Table 4: The angles for data collected between 05:15:30 and 05:35:30 UT between the spacecraft's separation line and the wave vector projection

sat13x	sat13y	sat13z	sat23x	sat23y	sat23z	sat43x	sat43y	sat43z
91.019	89.999	91.105	180	129.283	0	180	96.493	0
88.440	89.707	89.458	0	84.6861	180	0	82.169	180
87.744	90.373	88.430	0	93.4974	0	0	95.4253	0
87.531	90.307	88.349	0	137.564	0	0	111.0154	0
87.9396	89.4614	88.5356	0	70.777	0	0	69.3972	0
90.6963	89.7455	92.3431	0	55.6499	0	0.4231	72.1716	180
89.7298	90.3748	88.9727	0.9572	90.7195	0.7554	0.9156	90.6354	0.8758
90.1759	89.8234	90.4087	0.8956	90.0073	0.8693	0.9042	89.8491	0.8924
90.1656	89.9042	89.0386	0.8971	89.7027	0.9101	0.8997	89.8909	0.8961
89.4871	89.8981	88.8205	0.8936	89.267	0.8668	0.8959	89.6956	0.8861
89.3064	90.46	88.9975	0.8808	91.1998	0.8659	0.8894	90.5848	0.8834
89.7205	89.9964	88.5129	0.8977	90.4093	0.8826	0.8989	90.1433	0.8864
90.6764	90.0316	93.6282	0.9059	89.9652	0.8581	0.9063	90.0517	0.946
89.3357	89.9646	88.0846	0.8955	89.9787	0.9515	0.8962	89.9522	0.8844
89.4179	89.9397	88.5015	0.8736	89.8535	0.8475	0.8884	89.8837	0.8747
89.4422	90.0793	89.3962	0.8807	90.3029	0.8575	0.8902	90.204	0.8799
89.541	89.6709	89.4208	0.9125	89.1076	0.9097	0.9034	89.4838	0.9046
90.5621	90.0322	89.5058	0.8839	90.1258	0.8858	0.8964	89.996	0.8913
89.9286	90.0582	90.5294	0.9062	89.9535	0.8945	0.9012	90.1576	0.904

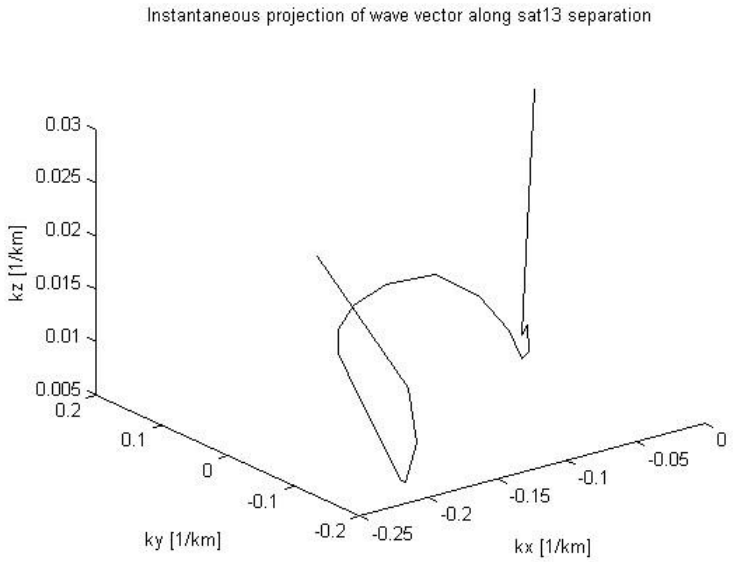

Figure 8: Instantaneous projection of wave vector along sat13 separation.

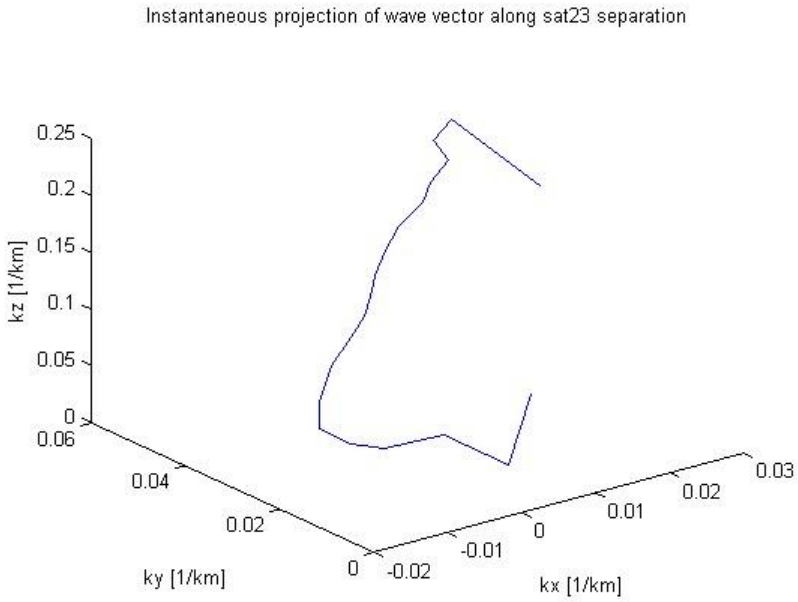

Figure 9: The wave vector projected instantly along the Sat23 separation.

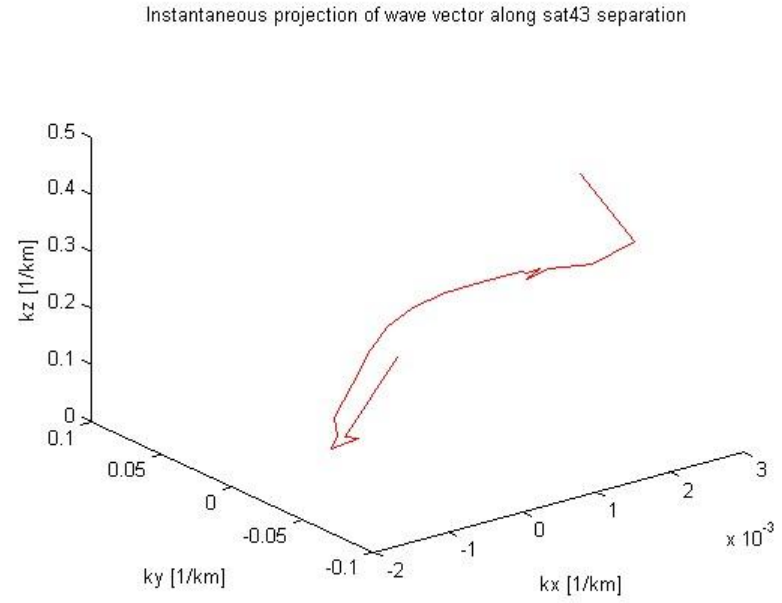

Figure 10: The wave vector projected instantly along the Sat43 separation.

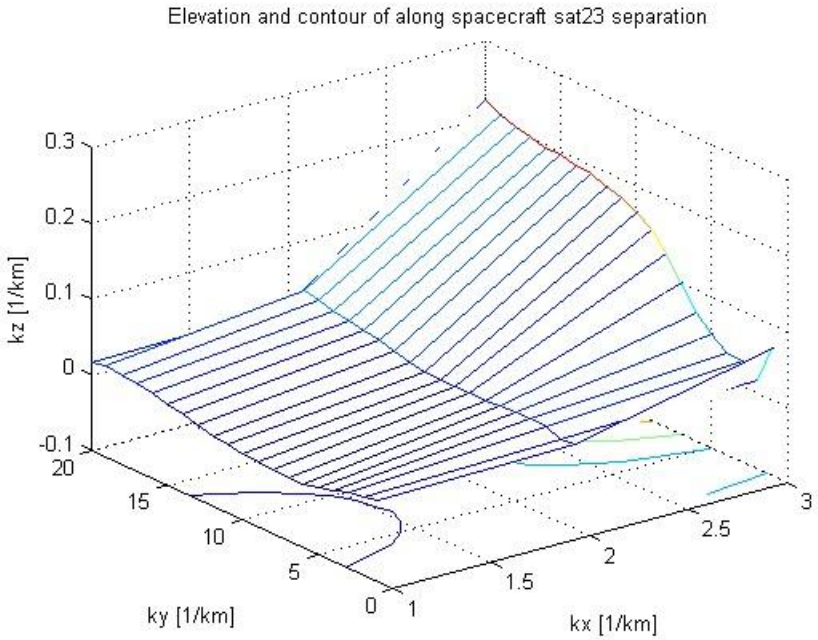

Figure 11: Wave vector projection's elevation and contour along the Sat23 separation.

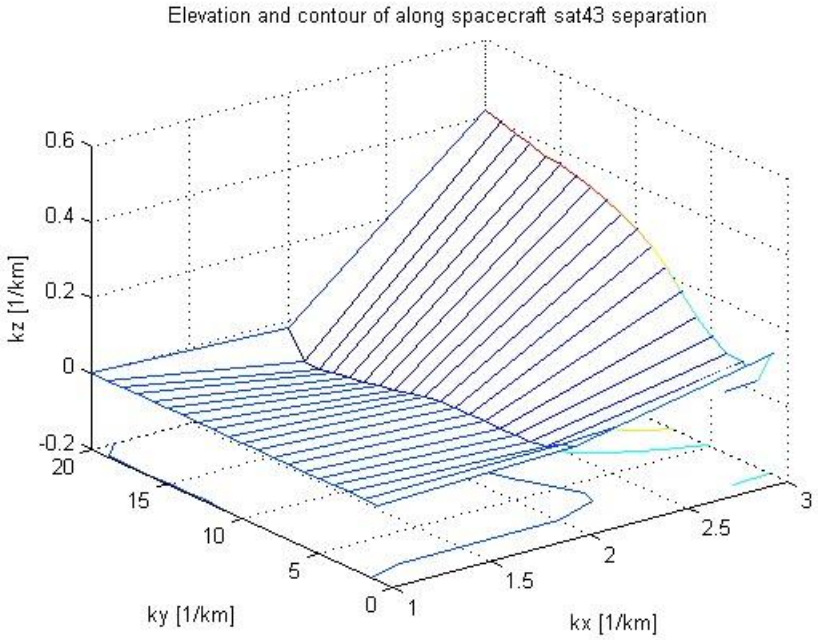

Figure 12: The wave vector's elevation and contour along the Sat43 separation.

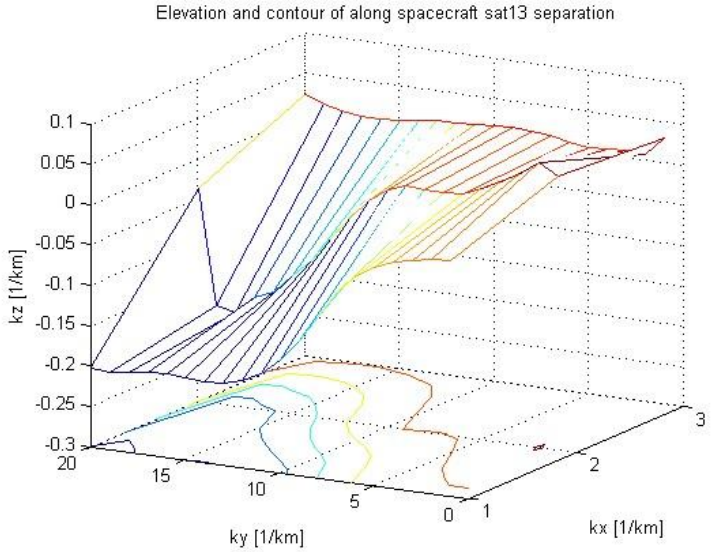

Figure 13: The wave vector's elevation and contour along the Sat13 separation.

Table 5: Components of wave vector along the separation of spacecraft

t [h:m:s]	k13x	k13y	k13z	k23x	k23y	k23z	k43x	k43y	k43z
05:15:30	0.0208	-.3664	0.0013	-.0001	0.0005	0.0006	0.001	-.0003	0.0032
05:16:30	-.0201	-.3713	0.0181	0.0032	0.0004	-.0068	0.0017	-.0003	-.0066
05:17:30	-.0072	-.3791	-.0024	0.002	-.0003	0.0044	0.0015	0.0009	0.0084
05:18:30	-.0043	-.3722	-.0021	0.0025	0.0008	0.0037	0.0019	-.0011	0.0073
05:19:30	-.0043	-.3804	-.0026	0.0035	0.0005	0.0037	0.0024	-.0015	0.0069
05:20:30	-.0067	-.3874	-.0018	0.0039	-.0018	0.0034	0.0025	0.0027	0.0057
05:21:30	0.0215	-0.387	-.0077	-.0016	-.0006	-0.114	-0.001	0.0007	-0.192
05:22:30	0.0006	-.3881	-.0058	0.0061	0.0011	-.1597	0.0022	-.0023	-0.283
05:23:30	-.0023	-.3932	0.0016	0.0009	-.0004	-.1697	0.0002	0.0009	-.3019
05:24:30	0.0014	-.3962	-.0032	-.0001	0	-.1565	-.0005	-.0003	-.2796
05:25:30	-.0026	-.3934	-.0041	0.0006	0.0005	-.1595	0.0002	-.0013	-.2857
05:26:30	0	-.3959	-0.002	0.0016	0.0005	-.1594	0.0012	-.0004	-.2853
05:27:30	-.0038	-.4036	-.0053	0.0016	-.0001	-.1524	0.001	0.0001	-.2741
05:28:30	0.0006	-.4067	-0.003	-.0011	0.0005	-.2381	-.0007	-.0011	-.4236
05:29:30	-.0045	-.4087	-.0045	0.0008	0	-.1555	0.0005	0.0001	-.2837
05:30:30	0.0011	-.4104	-.0017	-.0003	-.0004	-.1559	-.0002	0.001	-.2841
05:31:30	0.0045	-.4166	0.0051	-.0001	0.0001	-.1566	0.0001	-.0004	-.2853
05:32:30	-.0105	-.4174	-.0021	0.0022	-.0006	-.1561	0.0014	0.0013	-.2864
05:33:30	0.0072	-.4186	-0.001	-.0014	-.0012	-.1536	-0.001	0.0024	-.2834
05:34:30	0.0037	-.4243	0.0009	0.0001	0.0004	-0.162	0.0006	-.0009	-.2992

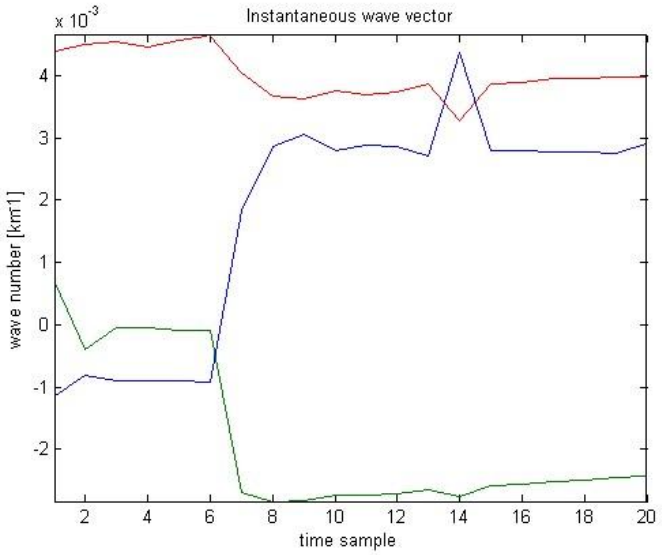

Figure 14: The wave number projected instantaneously as a function of time. Time is in second.

Table 6: Instantaneous wave vector for 35 MHz mean frequency wave propagation, expressed in (kilometers)$^{-1}$

t [h:m:s]	k_x	k_y	k_z	k
05:15:30	-0.0011	0.0007	0.0044	0.0046
05:16:30	-0.0008	-.0004	0.0045	0.0046
05:17:30	-0.0009	0	0.0046	0.0046
05:18:30	-0.0009	0	0.0045	0.0046
05:19:30	-0.0009	-.0001	0.0046	0.0047
05:20:30	-0.0009	-.0001	0.0046	0.0047
05:21:30	0.0018	-.0027	0.004	0.0052
05:22:30	0.00297	-.0028	0.0037	0.0054
05:23:30	0.0031	-.0028	0.0036	0.0055
05:24:30	0.0028	-.0027	0.0038	0.0054
05:25:30	0.0029	-.0027	0.0037	0.0054
05:26:30	0.0029	-.0027	0.0037	0.0054
05:27:30	0.0027	-.0026	0.0039	0.0054
05:28:30	0.0044	-.0028	0.0033	0.0061
05:29:30	0.0028	-.0026	0.0039	0.0054
05:30:30	0.0028	-.0026	0.0039	0.0054
05:31:30	0.0028	-.0025	0.0039	0.0054
05:32:30	0.0028	-.0025	0.004	0.0054
05:33:30	0.0027	-.0025	0.004	0.0054
05:34:30	0.0029	-.0024	0.004	0.0055

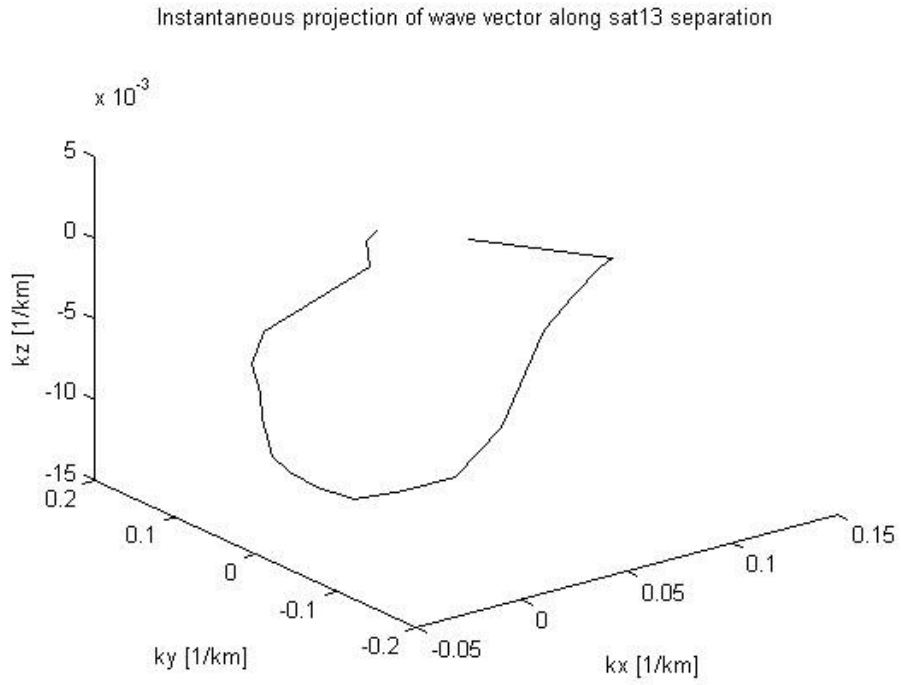

Figure 15a: Wave vector instantaneously projected along Sat13 separation

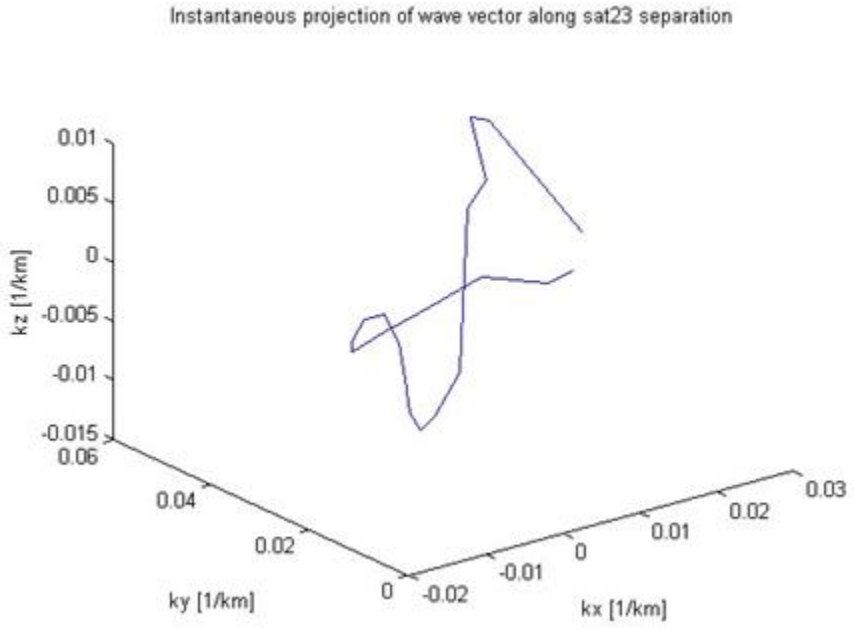

Figure 15b: Wave vector's instantaneous projection along Sat23 separation.

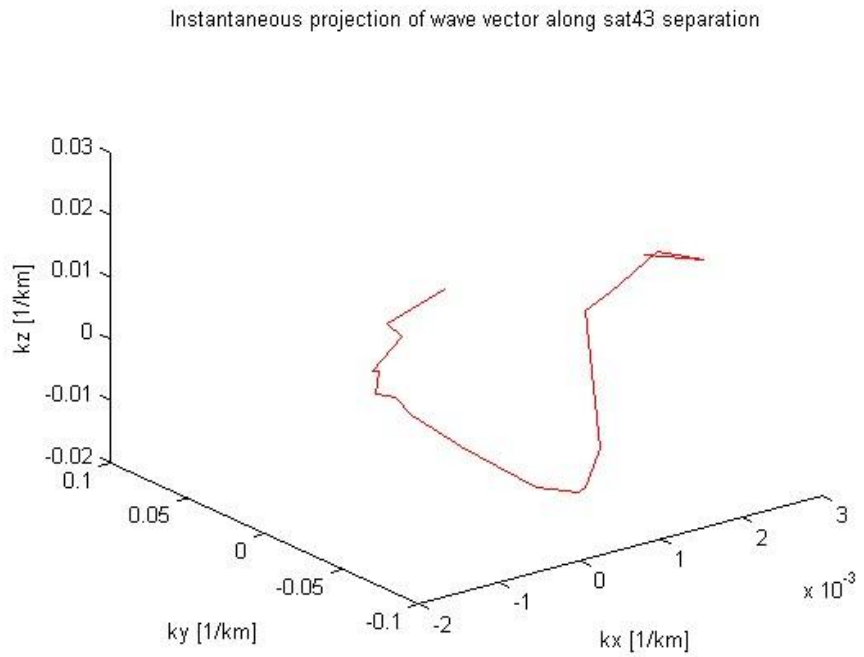

Figure 15c: Wave vector instantaneously projected along Sat43 separation

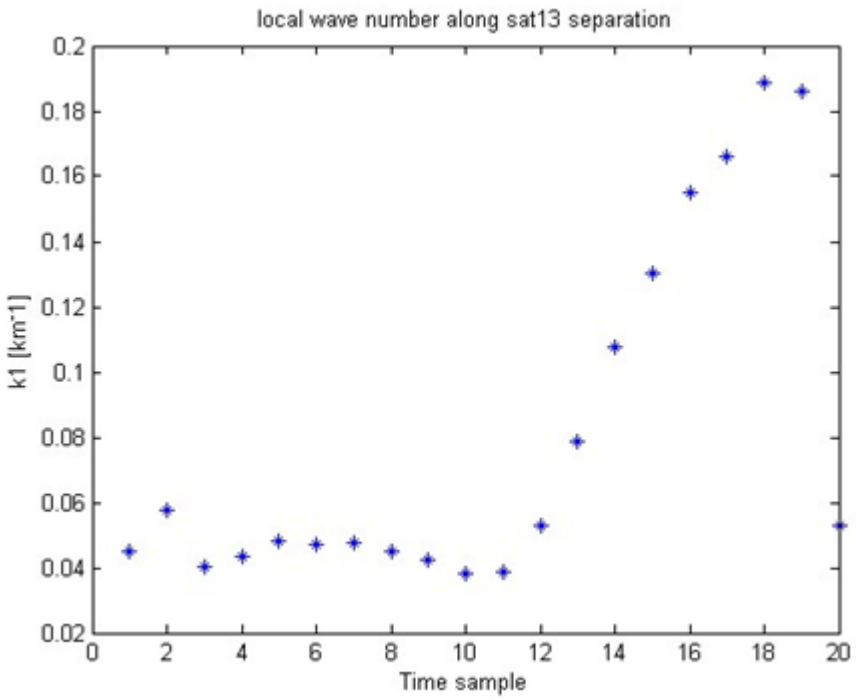

Figure 16a: Local wave number along Sat13 separation

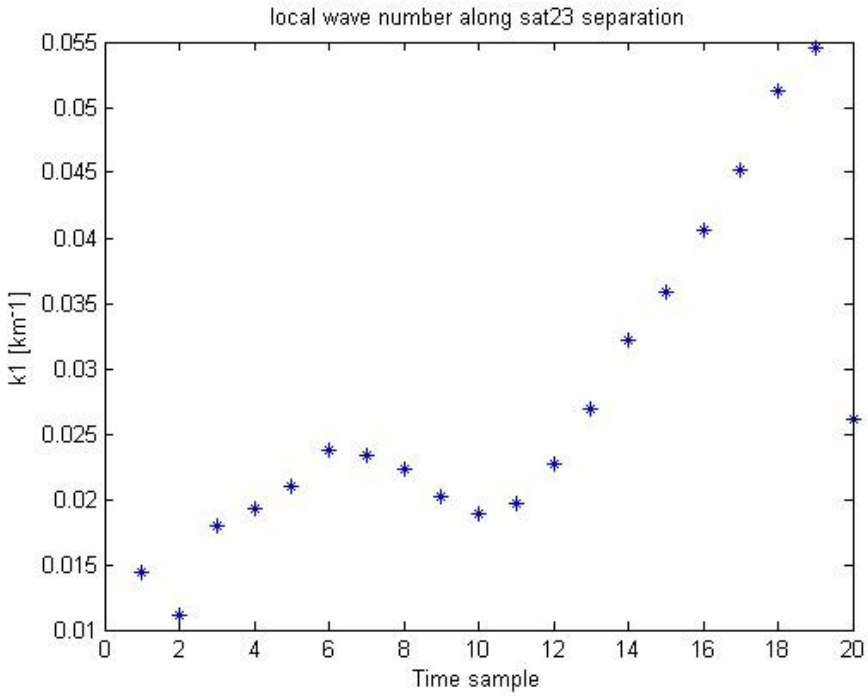

Figure 16b: Local wave number along the separation of Sat23

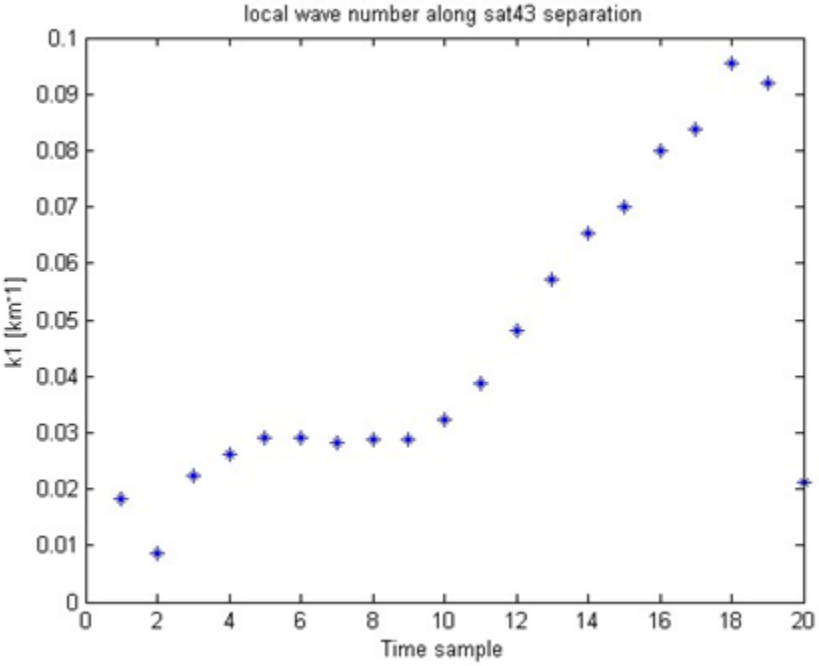

Figure 16c: Local wave number along sat43 separation.

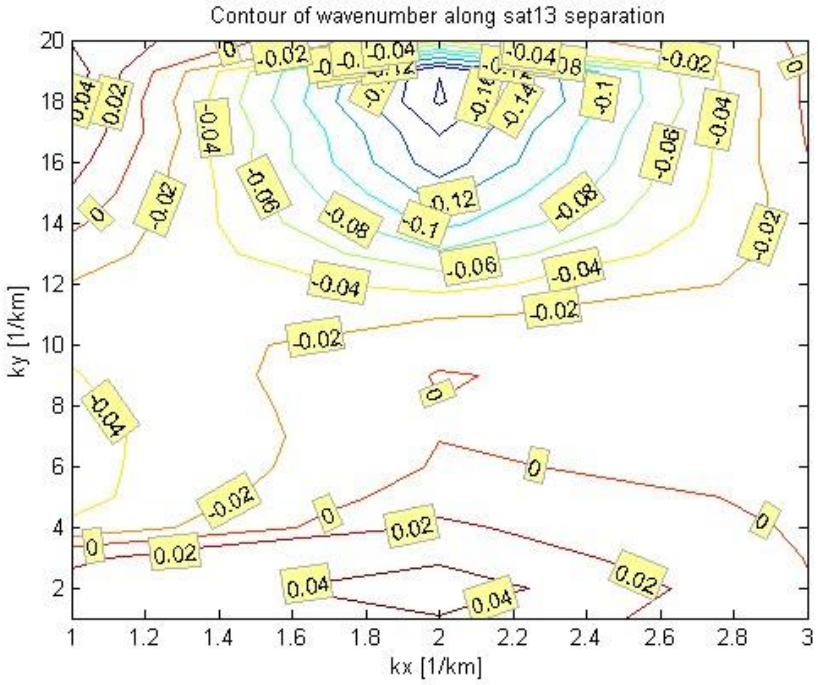

Figure 17a: The contour of the wave vector projection along the Sat13 separation, showing the instantaneous frequencies

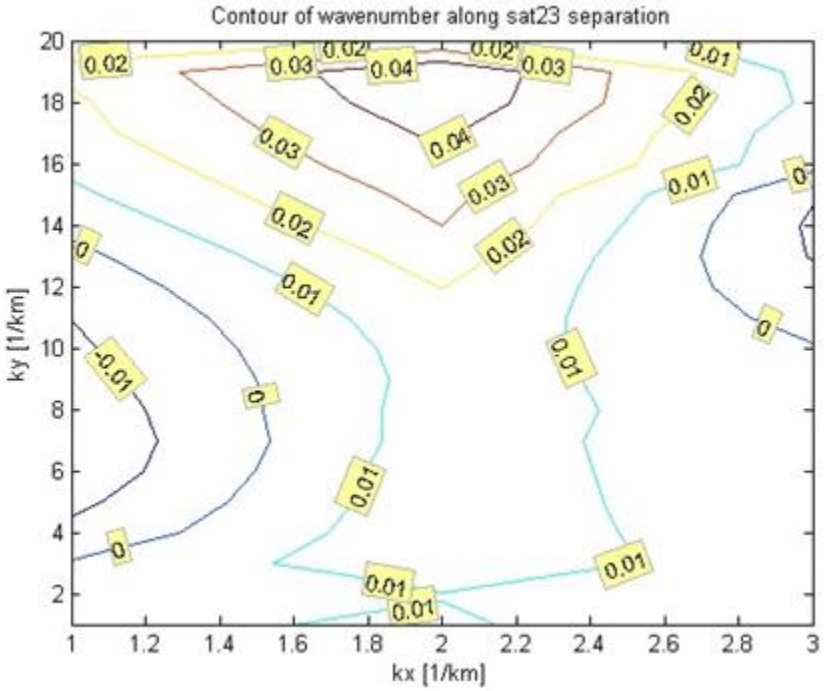

Figure 17b: The contour of the wave vector's projection along the Sat23 separation, displaying instantaneous frequencies.

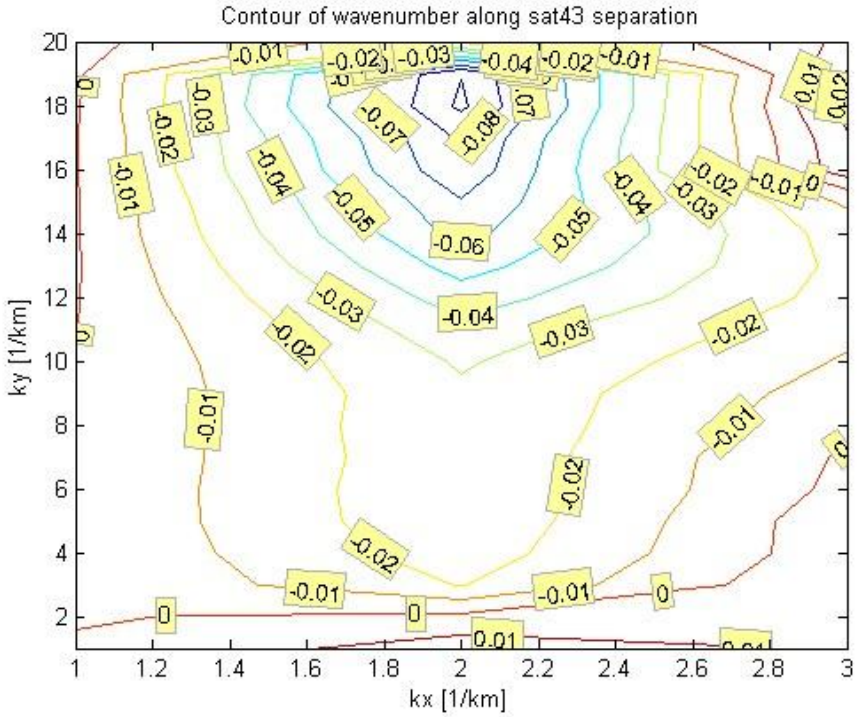

Figure 17c: The contour of the wave vector projection along the Sat43 separation, showing the instantaneous frequencies

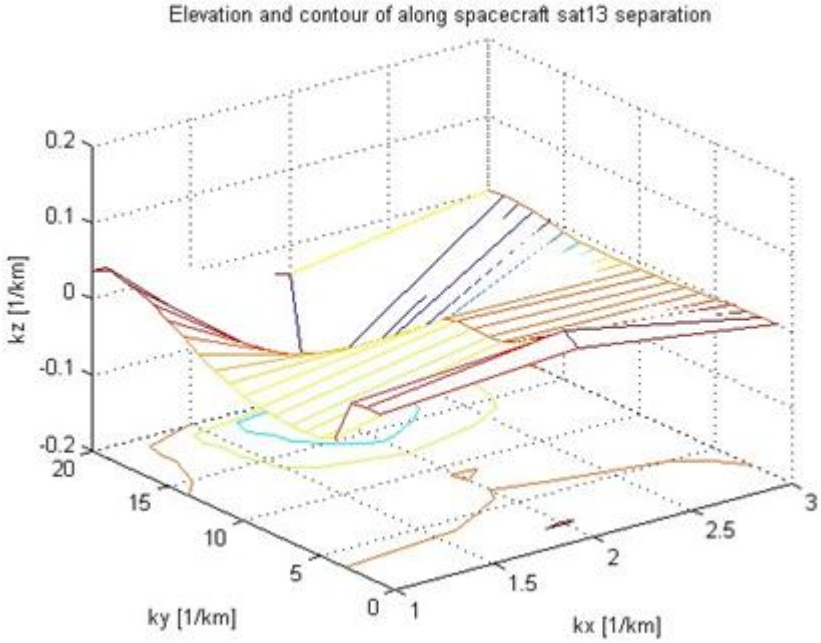

Figure 18a: Wave vector projection's elevation and contour along the Sat13 separation.

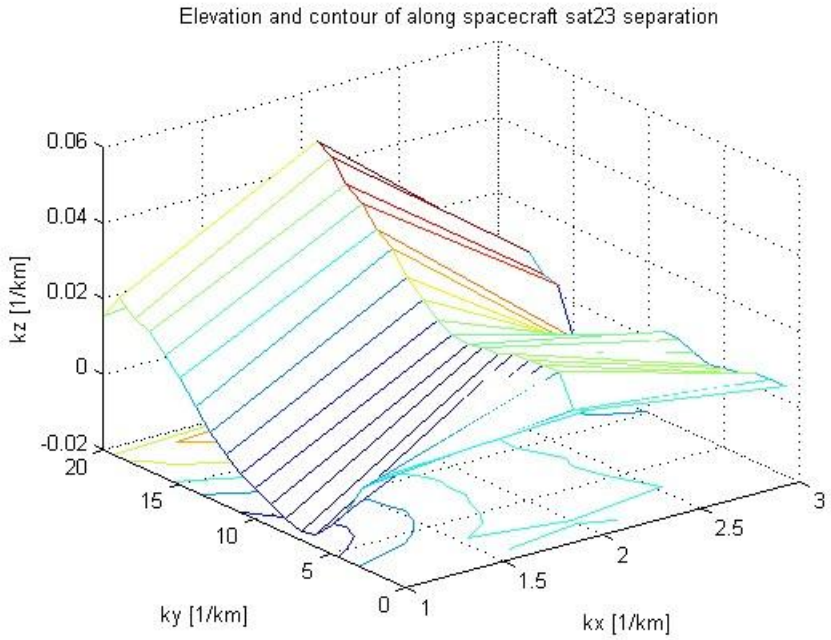

Figure 18b: Wave vector projection's elevation and contour along the Sat23 separation

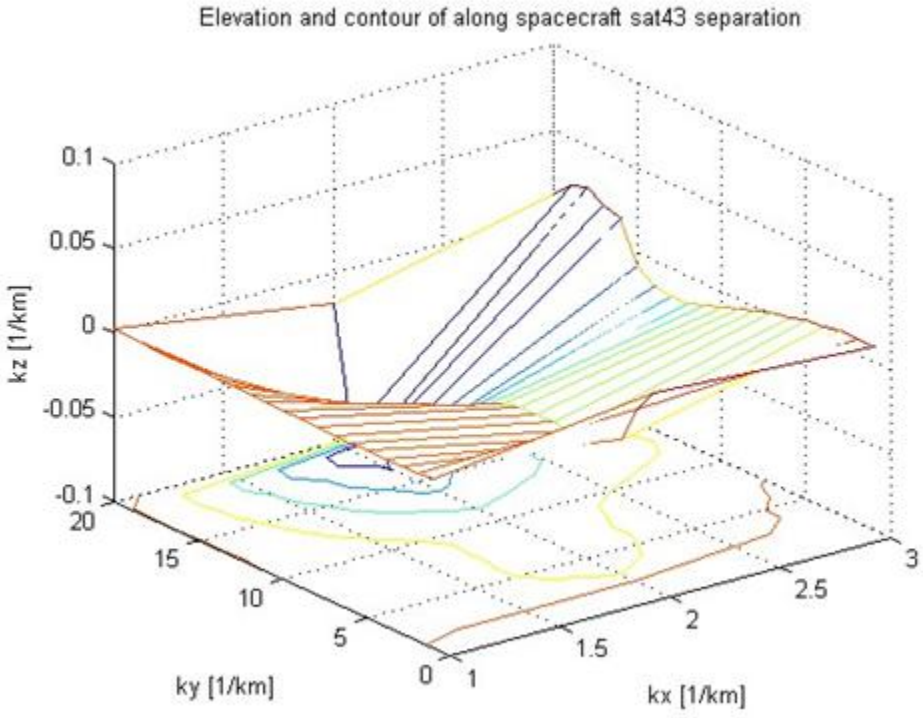

Figure 18c: The contour and elevation of the wave vector projection along the Sat43 separation

4.0 Discussion

The frequencies f1 and f2 [Hz] in Table 1 are the average local frequencies across 4 Spacecrafts as calculated from the x component of the chosen data. Two waves, f1 and f2, with instantaneous frequencies of [Hz], were seen. Additionally, two sets of instantaneous frequencies with a z− component were observed. However, we noticed

that the y-component only has one wave. According to our analysis, f2 is stable in both components, but f1 is unstable in the x and z-components. An anti-sunward flow in the x− direction is depicted by the velocities in Table 1.
The direction of the shock normal for waves propagating in the direction of the bow shock as seen by Cluster instruments C_1, C_2, C_3, and C_4 is displayed in Table 2 below using the minimum variance technique. In Table 2, first column displays the four Cluster spacecraft; the second column lists the eigenvectors for those four spacecrafts; the third column lists the smallest eigenvalues that correspond to those eigenvectors; and the fourth column displays the standard deviation of the magnetic field component along the estimated normal, which is calculated using the eigenvalues that appear in the third column.

The calculated results are nearly equal to the unit vector's magnitude in the normal direction, which is given as unity. As the four Cluster spacecraft crossed the bow shock, the eigenvectors in Table 2 represent the estimators for the vector normal to the shock. Moreover, the variation of the magnetic field component along the estimated normal is provided by the table's eigenvalue. The normal field component for this event varies with an average standard deviation of 1.271nT about the estimated normal as reported by C_1, C_2, C_3, and C_4 (1.319nT, 1.319nT, 1.354nT, and 1.395nT, respectively) as shown in Table 2.

The variance analysis uses Sonnerup and Cahill's (1967) work as a basis. Table 3 displays the direction of the highest, middle, and lowest variance for the observation that C_1 made. The C_1 satellite's data was chosen between 06:05:31 and 06:28:41 UT. The first column of Table 3 shows the total number of rows for the eigenvalues and eigenvectors that were calculated using the data's covariance matrix. The eigenvalue is shown in column two. The eigenvectors corresponding to the X, Y, and Z - components in the Cartesian coordinate system are represented by the third, fourth, and fifth columns. The product of the eigenvectors and the mean magnetic field is shown in the sixth column. The row with eigenvectors appropriate for the direction of the normal is indicated by the smallest value in the second column; in this example, it is 1.616. The orthogonality of the maximum, intermediate, and minimum variances is displayed in Figure 6. The direction of the maximum and intermediate variances is 90 degrees apart and tangential to the shock normal's plane, which is referred to as the bow shock normal in Figure 6. The direction of the minimum variance is associated with the normal magnetic field B_n.

The angles that are formed between the spacecraft separation line and the components of the wave vector projection along spacecraft separation are sat13x to sat43z, arranged from the first column to the last on Table 4. The values of these angles, which are in the X, Y, and Z GSE coordinate system, indicate that the wave vector's projection is perpendicular to the separation line. The separation line of the Sat13 pair and the projection of each wave vector component have an angle between them that ranges from 87^o to 91^o (Table 4). Table 4 indicates that, for satellite combinations, the wave's x and z components propagated parallel to the lines of separation, while the wave's y component propagated perpendicular to the lines of separation. The wave gradually moved away from the line, but it kept moving parallel to the x and z coordinates after that. Additionally, it was evident that the propagation direction of sat13 was perpendicular to x, y, and z. This indicates that the line dividing sat1 from sat3 passes through the origin of the sat1 coordinate system. The information in columns 4, 5, 6, 7, 8, and 9 supports our initial

claim that sat pairs 23 and 43 are observing in the same direction. Given that the angles in columns 4 and 7 are so tiny and so close to one another, we believe that the direction of propagation is parallel to the separation line.

The elements of the wave vector along the spacecraft separation are displayed in Table 5. Data were gathered for 20 minutes, from 05:15:30 to 05:35:30 UT. Equation 1 is used to calculate the outcomes shown in Table 5. For wave propagation with a mean frequency of 35 mHz. Table 6 displays the instantaneous wave vector. Based on the wave number, the wavelength of the wave is calculated and ranges from 1030.2 km to 1366.1 km (Table 6). Because of the turbulent behavior during the chosen period in the magnetosheath, special consideration must be given to the analysis technique chosen. The period includes the area near the magnetopause and the early arrival of waves near bow shock.

According to Nathaniel *et al*. (2013), the magnitude denotes a wave packet with non-stationary behavior that is readily explained by the superposition of multiple waves. The local wave vector projection has been plotted as shown in Figures 8 through 10 along the distance between the two spacecrafts, using the y - component, which we determined to be stable for frequency decomposition. Satellite pairs, also referred to as spacecraft or instrument pairs, are represented by the numbers sat13, which represents the combination of Cluster C_1 and C_3, sat23, which represents the combination of C_2 and C_3, and sat43, which represents the combination of C_4 and C_3. In this case, the satellite pairs 13, 23, and 43 can also be used to convey the same meaning. Spacecraft C_3 serves as our point of reference. The separation line between spacecraft C_1 and C_3 is perpendicular to the wave vector's projection, according to the instantaneous local wave vector analysis (Figure 5). The wave vector's instantaneous projection along the Sat13 and Sat43 separations exhibits a close pattern, as seen in Figures 8 and 10.

We also examined the contour and elevation of these wave vector projections and discovered that the contour and elevation of the wave vector projections along the Sat23 and Sat43 separations are similar in Figures 11 and 12. Plots of the wave vector's instantaneous projections show that satellite pairs 13 and 43 saw the same events, indicating that their positions are in an antiphase arrangement. It was established that satellite pair 23 recorded events differently from the other two pairs by comparing figures 9, 13, 15b, 16b, 17b, and 18b. Additionally, satellites 13 and 43 recorded quasi-similar events, as shown in Figures 8, 10, 15a, 15c, 16c, 17a, 17c, 18a, and 18c.

The propagation direction is therefore perpendicular as a result. We suspect a spiral kind of wave. The plot of the instantaneous wave number against time is shown in Figure 14. The similarity in the wave vector projection along the directions of the combination of sat13 (blue) and sat43 (green) is once again demonstrated by this, whereas sat23 (red) anti-correlated sat43. The distributions in the x and z components of figures 15–20 show that the projection of the x- and z-components are parallel to the separation line, as can be seen by examining the angle between the projection of each component of the wave vector of the Sat23 pair and Sat43 pair. Additionally, it demonstrates that the separation line is parallel to both the y-component of the wave vector projected for the sat23 pair and the sat43 pair. Further evidence that the Sat13 and Sat43 pairs can observe the same events with different positions is provided by the contours of Figures 17a, 16c, and 17c. The contour pattern in the figure

s is comparable to that of Figures 18a and 18c, which depict the contours and elevation of the instantaneous wave vector's projection along the pairs of Sat13 and Sat43. However, the Sat23 pairs are not the same.

The local wave number in Table 4, was plotted in Figures 16a and 16c, where the values of the wave vector projection showed the similarity between the Sat13 and Sat43 pairs. The non-dispersive direction of the Sat23 pair is also observed. Figure 14 illustrates the linearity of the wave vector component's projection on the separation line with respect to time. As a result, it suggests that the separation line and the Sat23 pair are oriented west-east or dawn-dusk. Additionally, it suggests that the separation line of the Sat43 pair points in the direction of the sun or north-south in the solar wind coordinate system.

5.0 Conclusion

In this paper, we have tried to analyze the plasma wave in order to determine the local wave vector orientation in the tetrahedral formation—the earth's magnetosheath—that spacecraft have observed. The period includes the area near the magnetopause and the early arrival of waves near bow shock. In this analysis, the geometry of the spacecraft is examined within a tetrahedral formation. For values small enough to permit a three-dimensional analysis, the tetrahedron's elongation (E) and planarity (P) were taken into consideration. Satellite separation, plasma bulk speed, and magnetic field data have all been made available through the use of cluster mission data. The instantaneous local wave vector analysis during the projection along satellite separation was made possible by these data. Multi-satellite observation was utilized to its full potential. The relevant data from the four Cluster satellite given as C_1, C_2, C_3 and C_4 were used. Taking into account the tetrahedral formation of the satellites with small E and P, these data produced three-dimensional results along each satellite pair separation.

The average minimum and maximum spacecraft separation, according to the results, were 88 and 108 km, respectively. The tetrahedral geometry of the four Cluster satellite on February 18, 2002, observed at 5: 27: 30 UT, yielded average values of E = 0.070 and P = 0.040 for a scale of 20.000km: 1.000cm. These values, used in this paper, compare favorably with those in Robert, A. et al., 1998, whose average values were reported as E = 0.076 ± 0.006 and P = 0.053 ± 0.004. Since the values of E and P for a regular tetrahedron are close to zero, these values are small enough to ensure good results of the 3 − D measurement. The average value of the plasma bulk velocity during the chosen period is [−175, 52, 112] kms^{-1}. The local wave vector projection has been plotted along the spacecraft separation. As a reference satellite, we used Cluster satellite C3. This made it possible to pair, and Sat13, Sat23, and Sat43 were used.

Two waves, f1 and f2, with instantaneous frequencies of [Hz], were seen. Two sets of instantaneous frequencies with a z− component were also observed by us. However, the y− component only has one wave. The wave's wavelength is between 1030.2 and 1366.1 kilometers. We also examined the elevation and contour of these wave vector projections, and from the plotted figures, we were able to determine that the wave vector projections along the Sat23 and Sat43 separations were similar in both respects. Plots of the wave vector's instantaneous projections show that satellite pairs 13 and 43 saw the same events, demonstrating that their locations indicate that the waves are arranged antiphase. The separation line between spacecraft C1 and C3 is found to be

perpendicular to the wave vector's projection, according to the instantaneous local wave vector analysis. Between the separation line of the Sat13 pair and the projection of each wave vector component, there is an angle that ranges from 87 to 91 degrees. Additionally, it was clear that the propagation direction of sat13 was perpendicular to x, y, and z. This indicates that the line dividing sat1 and sat3 passes through the origin of the sat1 coordinate system. We believe the wave to be spiral-shaped.

The distributions in the x and z components show that the projection of the x- and z-components are parallel to the separation line, which is supported by the analysis of the angle between the projection of each component of the wave vector of the sat23 pair and sat43 pair. The projection of the x- and z- components are parallel to the separation line, as seen by the distributions in the x and z-components, according to an analysis of the angle between the projection of each component of the wave vector of the sat23 pair and sat43 pair. As a result, it suggests that the separation line and the Sat23 pair are oriented west-east or dawn-dusk. Additionally, it suggests that the separation line of the Sat43 pair points in the direction of the sun or north-south in the solar wind coordinate system. Thus, multi-satellite observations enabled analysis of the local wave vector orientation of plasma wave in the Earth's Magnetosheath observed by spacecraft in the tetrahedral formation.

Conflict of interest statement

There is no conflict of interest among the authors of this manuscript.

References

Balikhin, M. A., Dudok de Wit, T., Alleyne, H. St. C. K., Krasnosel´skikh, V., Mier-Jedrzejeowicz, W. A. C. and Baunmjohann W. (1997a). Experimental determination of the dispersion of waves observed upstream of quasiperpendicular shock. Geophysical Research Letter, 24, NO. 7:787–790.

Balikhin, M. A., Woolliscroft, L. J. C., Alleyne, H. St. C., Dunlop, M., and Gedalin, M. A. (1997b). Determination of the dispersion of low-frequency waves downstream of quasi-perpendicular shock. Ann. Geophysicae, 15:143–151.

Balogh, A., Dunlop, M. W., Cowley, S. W. H., Southwood, D. J., Thomlinson, J. G., Glassmeier, K. H., Musmann, G., Luhr, H., Buchert, S., Acun´a, M. H., Fairfield, D. H., Slavin, J. A., Riedler, W., Schwingenschuh, K. and Kivelson, M. G. (1997). The cluster magnetic field investigation. Space Sci. Rev., 79:65 – 92.

Balogh, A., Schwartz, S. J., Bale, S. D., Balikhin, M. A., Burgess, D., Horbury, T. S. (2005). Cluster at the bow shock: Introduction. Space Science Reviews, 118(1–4), 155–160. https://doi.org/10.1007/s11214-005-3826-1.

Beall, J. M., Kim, Y. C. and Powers, E. J. (1982). Estimation of wavenumber and frequency spectra using fixed probe pairs. J. Appl. Physics, 53:3933–3940.

Boashash, B. (1992). Estimating and interpreting the instantaneous frequency of a signal-part 1: Fundamentals. Proc. IEEE, 80, No. 4:520–538.

Carozzi, T. D., Buckley, A. M. and Gough, M. P. (2004). Instantaneous wave vector estimation from multi-spacecraft measurements using few spatial points. Annales Geophysicae, 22:2633–2641.

Nathaniel, E.U., George, N.J. and Etuk, S.E. (2013). Determination of Instantaneous

Frequencies of Low Plasma Waves in the Magnetosheath using Empirical Mode Decomposition (EMD) and Hilbert Transform (HT). Atmospheric and Climate Sciences, 3, 576-580.

Nathaniel, E.U., George, N.J., Ibanga, J.I and Ekanem, A.M. (2016). Efficacy of Hilbert-Huang Transform (HHT) in the analysis of instantaneous low frequency waves of Magnetosheath. International Journal of Geosciences, 7, 11-19.

Flandrin, P., Rilling, G. and Goncalves, P (2004.). Empirical mode decomposition as a filter bank. IEEE Signal Process. Lett., 11, no. 2:112–114.

Gabor, D. (1946). Theory of communication. Jour. IEE, 93, Part III, No. 26:429–457.

Glassmeier, K. H., Motschmann, U., Dunlop, M., Balogh, A., Acun´a, M. H., Carr, C., Musmann, G., Fornacon, K.H., Schweda, K., Vogt, J., Georgescu, E. and Buchert S. (2001). Cluster as a wave telescope- first results from the fluxgate magnetometer. Ann. Geophysicae, 19:1439–1447.

Helong, L., Xiaoyan D. and Hongliang D. (2007). Structural damage detection using the combination method of EMD and Wavelet analysis. Mechanical Systems and Signal Processing, 21:298–306.

Huang, N. E., Shen, Z., Long, S. R., Wu, M. C., Shih, H. H., Zheng, Q., Yen, N., Tung, C. C. and Liu, H. H. (1998). The empirical mode decomposition and the Hilbert spectrum for nonlinear and non-stationary time series analysis. Proc. R. Soc. Lond. A, 454:903–995.

Huang, N. E., Wu, M., Qu, W., Long, S. R. and Shen S. S. P. (2003). Applications of Hilbert-Huang transform to non-stationary financial time series analysis. Appl. Stochastic Models Bus. Ind., 19:245–268.

Huang, N. E. and Shen, S. S. (2005). Hilbert - Huang Transform and its applications. World Scientific Publishing Co. Pte Ltd., Singapore.

Nathaniel, E U., Beloff, N. and George, N.J. (2013). Instantaneous frequency and wave mode identification in a magnetosheath using few spatial points. Chin. Phys. B, Vol. 22, No. 8

Paschmann, G., Haerendel, G., Sckopke, N., Mobius, E., Luhr, H. and Carlson C. W. (1988). Three-dimensional plasma structure with anomalous flow directions near the earth's bow shock. J. Geophysical Research Letter, 93:11279–11294.

Pinco`n, J. L., and Lefeuvre, F. (1991). Local characterisation of homogeneous turbulence in a space plasma from simultaneous measurements of field components at several points in space. J. Geophys. Res. lett., 96:1789.

Rilling, G. and Flandrin, P. (2006). On the influence of sampling on the empirical mode decomposition. IEEE, page 4.

Robert, P., Roux, A., Harvey, C. C., Dunlop, M. W., Daly, P. W. and Glassmeier, K. H. (1998). Analysis methods for multi-spacecraft data (tetrahedron geometric factors). Int. Space Sci. Inst., Bern, Switzerland, pages 323–348.

Svenningsson, I., Yordanova, E., Cozzani, G., Khotyaintsev, Yu. V., & André, M. (2022). Kinetic generation of whistler waves in the turbulent magnetosheath. Geophysical Research Letters, 49, e2022GL099065.

https://doi. org/10.1029/2022GL099065.

Sonnerup, B.U.O. and Cahill, L. J. (1967). Magnetopause structure and attitude from explorer 12 observations. J. Geophys. Res. lett., 72, No. 1:171–183.

Walker, S. N., Sahraoui, F., Balikhin, M. A., Belmont, G., Pincon, J. L., Rezeau, L., Alleyne, H., Cornilleau-Wehrlin, N. and Andr´e, M. (2004). A comparison of wave mode identification techniques. Anales Geophysicae, 22:3021–3032.

CDA - Http://cdaweb.gsfc.nasa.gov/cgi-bin/eval-2.cgi.